Macro-modelling of orthotropic damage in masonry: Combining micro-mechanics and continuum FE analysis

Anastasios Drougkas

School of Civil Engineering, University of Leeds, Woodhouse Lane, LS2 9JT Leeds, United Kingdom
Serra Húnter Fellow, Department of Strength of Materials and Structural Engineering, Universitat Politècnica de Catalunya (UPC-BarcelonaTech), C/ Colom 11, 08222 Terrassa, Spain

1. Introduction

Due to the complex interaction of its constituent materials, arising from their brittleness and staggered geometric arrangement, masonry as a composite material is often characterised by pronounced orthotropy, both in elasticity and strength [20]. This orthotropy is particularly important in the study of earthquake induced damage and collapse mechanisms of large masonry structural elements [23]. Accurate prediction of the force capacity of masonry elements, therefore, relies not only on the careful mechanical characterisation of its comprising materials, but also on modelling their interaction at the material scale [32].

Finite element (FE) analysis of masonry structures can assume different levels of detail for the representation of the mechanical features and potential failure modes of the material. For example, in a macro-modelling approach the material may be treated as an isotropic [7] or orthotropic [26] continuum. The large number of material parameters in need of characterisation for the execution of these simulations has led to the development of experimental frameworks [12], empirical approaches [11] and numerically-driven calibration methods [16] for determining these parameters. While both approaches have been successfully used for nonlinear analysis [8,21,28], it is the latter that provides a truer representation of the mechanical properties of masonry. Continuum modelling can be very attractive due to the geometrical simplicity of the resulting models and the reduced computational costs, especially for modelling large structures. However, orthotropic models must still rely on complex experiments, well-founded assumptions or ancillary computations for actually determining the orthotropic properties of the continuum.

Stemming from the inherent attractiveness of continuum modelling and the need for deriving macroscopic orthotropy from materials that are themselves often isotropic, constitutive approaches have been developed for taking into account the interaction of potential failure modes in regularly bonded masonry through a phenomenological or analytical rather than a detailed micro-mechanical approach [27,29]. While very promising, this approach does not directly provide comprehensive information on the stresses and strains in the material components comprising the masonry composite.

Meso-modelling, meaning the simulation of the masonry joints with interface elements connecting continuum units, is an approach that allows the direct representation of the masonry geometric bond and only relies on the mechanical characterisation of the constituent materials [18,25]. Orthotropy arises directly from the geometric interlocking of the units without any assumptions regarding material properties of the masonry or of its components. Additionally, tensile failure of the units can be considered through the inclusion of interface elements across their mid-length. Overall, this approach is well suited to capturing the behaviour of masonry as it is affected by its geometric bond, be it regular or irregular. However, the geometric representation of the units is not exact, numerical integration of non-linear interface elements is often unstable and the approach does not easily allow complex biaxial interaction of stresses to be introduced in the failure criterion for the units.

Further increasing the level of detail, micro-modelling directly incorporates separate geometric representations of the units and the mortar, with or without the use of nonlinear interfaces between the material phases, into the continuum model [11,14]. This approach allows the direct simulation of all potential failure types that can arise in the units, mortar and the unit-mortar interface. However, the computational cost can be very high due to the fineness of the mesh required for attaining the desired level of geometric detail. Further, interpretation of the results is often cumbersome due to the amount of results data produced. It is thus not common practice to use this approach for nonlinear analysis of full structures.

In response to the high computational cost of FE micro-modelling, one may resort to micro-mechanical approaches for the solution of simple linear [5,10,31,33] and nonlinear [13,30,34] elasticity problems. Bespoke solutions for different types of masonry geometric bonds can be produced and solved with reduced computational effort, even for nonlinear analysis. In turn, these models provide a solid basis for two-scale analysis of larger structures.

In this paper it is attempted to combine micro-mechanical methods for modelling the interaction of the material phases in the masonry composite with nonlinear constitutive laws for tension, compression and shear in the context of FE macro-modelling, thus achieving comprehensive results in terms of stress, strain and damage distribution in the units and the joints while maintaining the computational cost at a low level.

The proposed model is based on the analysis of a masonry periodic unit cell for the determination of the stress and strain distribution in the units and joints. These stresses and strains are used for evaluating the damage to the units and joints through the adoption of nonlinear constitutive laws. Finally, the cells are employed for driving a two-scale analysis of masonry structures. A series of experimental tests on scaled masonry walls subjected to in-plane shear under different levels of vertical pre-compression is used for evaluating the accuracy of the model in terms of predicted peak force and failure mode.

2. Analysis of masonry periodic unit cell

A masonry periodic unit cell is the smallest repeating geometrical entity representative of the geometric pattern of a masonry structure. Such geometric patterns are commonplace in regularly bonded brick masonry walls and include running, English and Flemish bonding patterns, to mention some of the most common. Such patterns are also encountered in cut stone masonry, but are far less common due to the higher cost of obtaining and cutting the material. The derivation of a running bond quarter cell is shown in Fig. 1, from the wall geometry, to the identification of the repeating pattern to, finally, the cell from geometrical symmetry of the bonding pattern. The adoption of a quarter vs a full cell as the basis of the homogenisation scheme, which can lead to alternating normal microscopic stresses in neighbouring components under pure shear macroscopic loading due to the antisymmetry of shear loads [35], is justified in the model validation subsection. The figure also illustrates the orientation of the masonry panel compared to the adopted Cartesian coordinate system: *x* for the horizontal direction and *y* for the vertical.

Regular bonding patterns in masonry panels produce simply identifiable geometric components in the cell, all with a rectangular shape. Each rectangle can be clearly associated with a material phase, either unit or mortar. This simple derivation of the rectangles composing the cell lends itself well to the adoption of a method-of-cells approach [1] for the analysis of the masonry composite material. The resulting rectangular components in a running bond cell and their naming convention is shown in Fig. 2. These components are: the head joints (h), two components for the units (u_1 and u_2), the cross joints (c) and the bed joints (b), arranged in horizontal rows and vertical columns. The dimensions are also indicated in the figure, with l_m being the thickness of the head joint, l_u the length of the unit, h_m the thickness of the bed joint and h_u the height of the unit.

The model for the analysis of the cell is based on the running bond model presented in a previous work [10]. A modification is
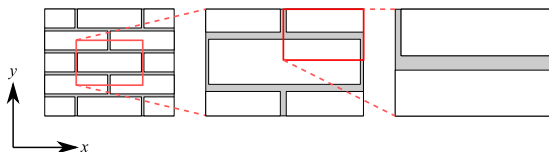

Fig. 1. Derivation of running bond periodic unit cell from running bond wall to repeating pattern to cell derived from symmetry of the pattern.
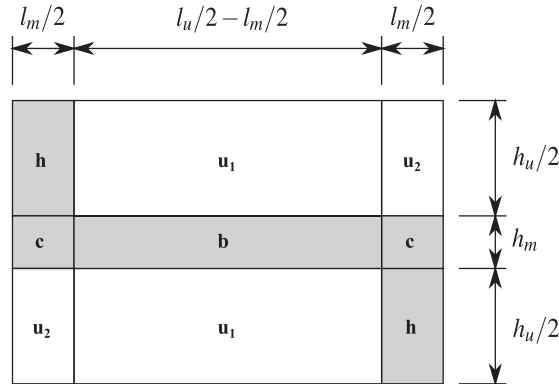
Fig. 2. Naming convention and dimensions for rectangular components of the running bond periodic unit cell.

introduced in the model developed in the present work. A plane stress condition is here assumed, meaning that out-of-plane stresses are disregarded in the analysis. Due to the present work's aim at modelling shear walls rather than pure compression of masonry wallettes, as was the goal in the previous work, modelling the additional confinement of the mortar by out-of-plane stresses was not deemed critical.

The analysis of the cell is based on simple analytical expressions for describing the interaction of the components in terms of stress equilibrium and strain conformity, further assuming that each component has constant stress and strain. These analytical expressions introduce the advantages of very low computational cost and simple interpretation of the interaction of the components. For the formulation of the system of analytical expressions, stress σ and strain ε components are noted using a subscript indicating the direction and a superscript indicating the component, while a lack of superscript corresponds to the cell, or macro, stress and strain.

Horizontal stress equilibrium is taken at the left edge and at a vertical cross-section across the centre of the cell:

$$\sigma_{xx}(h_m + h_u) = \sigma_{xx}^{u_2}\frac{h_u}{2} + \sigma_{xx}^{c}h_m + \sigma_{xx}^{h}\frac{h_u}{2}$$

$$\sigma_{xx}(h_m + h_u) = \sigma_{xx}^{u_1}h_u + \sigma_{xx}^{b}h_m \tag{1}$$

Vertical stress equilibrium is taken at the top edge and at a horizontal cross-section at the centre of the cell:

$$\sigma_{yy}\left(\frac{l_m}{2} + \frac{l_u}{2}\right) = \sigma_{yy}^{h}\frac{l_m}{2} + \sigma_{yy}^{u_1}\left(\frac{l_u}{2} - \frac{l_m}{2}\right) + \sigma_{yy}^{u_2}\frac{l_m}{2}$$

$$\sigma_{yy}\left(\frac{l_m}{2} + \frac{l_u}{2}\right) = \sigma_{yy}^{c}l_m + \sigma_{yy}^{b}\left(\frac{l_u}{2} - \frac{l_m}{2}\right) + \sigma_{yy}^{u_2} \tag{2}$$

One normal stress assumption is made in the horizontal direction between the two unit components:

$$\sigma_{xx}^{u_1} = \sigma_{xx}^{u_2} \tag{3}$$

Shear stress equilibrium is taken at the left edge of the cell, across a vertical cross-section across the centre of the cell and at the top edge of the cell:

$$\sigma_{xy}(h_m + h_u) = \sigma_{xy}^{u_2}\frac{h_u}{2} + \sigma_{xy}^{c}h_m + \sigma_{xy}^{h}\frac{h_u}{2}$$

$$\sigma_{xy}(h_m + h_u) = \sigma_{xy}^{u_1}h_u + \sigma_{xy}^{b}h_m$$

$$\sigma_{xy}\left(\frac{l_m}{2} + \frac{l_u}{2}\right) = \sigma_{xy}^{h}\frac{l_m}{2} + \sigma_{xy}^{u_1}\left(\frac{l_u}{2} - \frac{l_m}{2}\right) + \sigma_{xy}^{u_2}\frac{l_m}{2} \tag{4}$$

One shear stress assumption is made between the head joint and adjoining unit component:

$$\sigma_{xy}^{h} = \sigma_{xy}^{u_1} \tag{5}$$

Deformation conformity in the horizontal direction is assumed between the two rows of components. Normal strains along *xx* are assumed to contribute to the horizontal deformation of the components. Shear strains in *xy* are also assumed to contribute to the horizontal deformation. This contribution is assumed to be equal to the shear strain multiplied by half the height of the component [10]. The contribution of the shear deformation, especially related to the deformation of the bed joint, provides the necessary reduction of stiffness of the cell in the horizontal direction, without which the cell becomes exceedingly stiff as the comparative stiffness of the mortar compared to that of the unit is reduced. Thus, the lack of normal-shear coupling [2] in the presence of

horizontally interlocking units, which is detrimental to the accuracy of homogenisation schemes proposed for masonry structures based on matrix-inclusion micromechanics [15], is addressed. Based on this assumption, deformation conformity in the horizontal direction reads:

$$\varepsilon_{xx}^h \frac{l_m}{2} + \varepsilon_{xx}^{u_1} \left(\frac{l_u}{2} - \frac{l_m}{2}\right) + \varepsilon_{xx}^{u_1} \frac{l_m}{2} + \left(\varepsilon_{xy}^h + \varepsilon_{xy}^{u_1} + \varepsilon_{xy}^{u_1}\right) \frac{h_u}{4} = \varepsilon_{xx}^c l_m + \varepsilon_{xx}^b \left(\frac{l_u}{2} - \frac{l_m}{2}\right) + \left(2\varepsilon_{xy}^c + \varepsilon_{xy}^b\right) \frac{h_m}{2} \tag{6}$$

Deformation conformity in the vertical direction is assumed between the columns of components. Shear deformation is disregarded in the vertical direction. As such, the conformity reads:

$$\varepsilon_{yy}^h \frac{h_u}{2} + \varepsilon_{yy}^c h_m + \varepsilon_{yy}^{u_2} \frac{h_u}{2} = \varepsilon_{yy}^{u_1} h_u + \varepsilon_{yy}^b h_m \tag{7}$$

Two assumptions are made regarding the normal strains in the horizontal direction:

$$\varepsilon_{xx}^{u_1} = \varepsilon_{xx}^b$$

$$\varepsilon_{xx}^h = \varepsilon_{xx}^c \tag{8}$$

and two in the vertical direction:

$$\varepsilon_{yy}^{u_1} = \varepsilon_{yy}^h$$

$$\varepsilon_{yy}^c = \varepsilon_{yy}^b \tag{9}$$

The cell strains are equal to:

$$\varepsilon_{xx} = \frac{\varepsilon_{xx}^h \frac{l_m}{2} + \varepsilon_{xx}^{u_1} \left(\frac{l_u}{2} - \frac{l_m}{2}\right) + \varepsilon_{xx}^{u_1} \frac{l_m}{2} + \left(\varepsilon_{xy}^h + \varepsilon_{xy}^{u_1} + \varepsilon_{xy}^{u_1}\right) \frac{h_u}{4}}{\frac{l_u}{2} + \frac{l_m}{2}}$$

$$\varepsilon_{yy} = \frac{\varepsilon_{yy}^h \frac{h_u}{2} + \varepsilon_{yy}^c h_m + \varepsilon_{yy}^{u_2} \frac{h_u}{2}}{h_u + h_m}$$

$$\varepsilon_{xy} = \frac{\varepsilon_{xy}^h \frac{h_u}{2} + \varepsilon_{xy}^c h_m + \varepsilon_{xy}^{u_2} \frac{h_u}{2}}{h_u + h_m} \tag{10}$$

Finally, the isotropic Hooke's law in plane stress is applied to all components under normal and shear stress:

$$\begin{bmatrix} \sigma_{xx}^k \\ \sigma_{yy}^k \\ \sigma_{xy}^k \end{bmatrix} = \frac{E^k}{(1 - \nu^k)^2} \begin{bmatrix} 1 & \nu^k & 0 \\ \nu^k & 1 & 0 \\ 0 & 0 & 1 - \nu^k \end{bmatrix} \begin{bmatrix} \varepsilon_{xx}^k \\ \varepsilon_{yy}^k \\ \varepsilon_{xy}^k \end{bmatrix} \tag{11}$$

where the superscript k refers to any of the cell components and its assigned Young's modulus E^k and Poisson's ratio ν^k. This last equation can in principle be replaced with an orthotropic elasticity equation in the case of units with clearly characterised orthotropic properties.

For any given known cell strains (ε_{xx}, ε_{yy}, ε_{xy}), the above expressions constitute a linear system of equations, with component stresses and strains and cell stresses as unknowns. This system can be solved to determine all unknown values with minimal computational cost for determining the stress and strain at all rectangular components of the cell, and of the cell itself, as a function of the cell strain.

3. Damage model for cell components

The rectangular components comprising the cell can fail in compression or tension. Additionally, the unit-mortar interface may fail in tension or shear. Knowing the strains, and therefore the effective stresses, in the components, these failure types can be evaluated for calculating the loss of stiffness in the components themselves and, consequently, in the cell.

A damage mechanics approach is adopted for calculating the reduction of stiffness due to compression, tension and shear. The effective stresses, which are proportional to the strains as per eq. (11), are multiplied with integrity variables, ranging from 1 for an intact material to 0 for a fully damaged material, in order to calculate the actual stresses.

For compression a combination of a bilinear hardening and an exponential softening curve is adopted. As such, the integrity variable in compression I_c^k for each cell component k as a function of the strain ε is equal to:

$$I_c^k(\varepsilon) = \begin{cases} 1 & \varepsilon_c^l \le \varepsilon \le 0 \\ \dfrac{f_c^k}{\sigma_e}\left(\dfrac{3\varepsilon_c^l - \varepsilon_c^p}{3\varepsilon_c^l - 3\varepsilon_c^p} - \dfrac{2\varepsilon}{3\varepsilon_c^l - 3\varepsilon_c^p}\right) & \varepsilon_c^p \le \varepsilon \le \varepsilon_c^l \\ \dfrac{f_c^k}{\sigma_e}\exp\left(-\dfrac{\varepsilon - \varepsilon_c^p}{\varepsilon_c^u}\right) & \varepsilon \le \varepsilon_c^p \end{cases} \tag{12}$$

where f_c^k is the compressive strength of the component (negative), σ_e is the effective stress and ε_c^l, ε_c^p and ε_c^u being the proportional limit strain, peak strain and ultimate strain in compression respectively. These are equal to:

$$\varepsilon_c^l = \frac{f_c^k}{3E^k}$$

$$\varepsilon_c^p = 5\varepsilon_l$$

$$\varepsilon_c^u = \frac{G_c^k}{f_c^k h} \tag{13}$$

where G_c^k is the compressive fracture energy and h is the bandwidth.

For tension a linear behaviour up to peak stress is assumed, followed by an exponential softening curve. Consequently, the integrity variable in tension I_t^k for each cell component k is equal to:

$$I_t^k(\varepsilon) = \begin{cases} 1 & 0 \le \varepsilon \le \varepsilon_t^p \\ \dfrac{f_t^k}{\sigma_e}\exp\left(-\dfrac{\varepsilon - \varepsilon_t^p}{\varepsilon_t^u}\right) & \varepsilon_t^p \le \varepsilon \end{cases} \tag{14}$$

where f_t^k is the tensile strength of the component (positive) and ε_t^p and ε_t^u being the peak strain and ultimate strain in tension respectively. These are equal to:

$$\varepsilon_t^p = \frac{f_t^k}{E^k}$$

$$\varepsilon_t^u = \frac{G_t^k}{f_t^k h} \tag{15}$$

where G_t^k is the tensile fracture energy.

Similarly as for tension, a linear behaviour is assumed up to peak stress, followed by an exponential softening curve for shear strength f_v. As such, the shear strength as a function of the strain is:

$$f_v(\varepsilon) = \begin{cases} f_{v0} & 0 \le |\varepsilon| \le \varepsilon_v^p \\ f_{v0}\exp\left(-\dfrac{|\varepsilon| - \varepsilon_v^p}{\varepsilon_v^u}\right) & \varepsilon_v^p \le |\varepsilon| \end{cases} \tag{16}$$

where f_{v0}^k is the initial shear strength of the component (positive) and ε_v^p and ε_v^u being the peak strain and ultimate strain for the shear strength respectively. These are equal to:

$$\varepsilon_v^p = \frac{1 + \nu^k}{E^k}f_{v0}^k$$

$$\varepsilon_v^u = \frac{G_v^k}{f_{v0}^k h} \tag{17}$$

where G_t^k is the tensile fracture energy. For the friction coefficient μ the constitutive relation reads:

$$\mu(\varepsilon) = \begin{cases} \mu_0 & 0 \le |\varepsilon| \le \varepsilon_v^p \\ \mu_0 + \dfrac{(\mu_R - \mu_0)(f_{v0} - f_v(\varepsilon))}{f_{v0}} & \varepsilon_v^p \le |\varepsilon| \end{cases} \tag{18}$$

where μ_0 and μ_R are the initial and residual values of the friction coefficient respectively. Finally, the integrity variable in shear I_v^k can be calculated as:

$$I_v^k(\varepsilon) = \begin{cases} 1 & 0 \le |\varepsilon| \le \varepsilon_V^p \\ \dfrac{|\sigma_n|\mu(\varepsilon) + f_{v0}\exp\left(-\dfrac{|\varepsilon| - \varepsilon_V^p}{\varepsilon_v^u}\right)}{\sigma_e} & \varepsilon_V^u \le |\varepsilon| \end{cases} \tag{19}$$

where σ_n is the compressive stress acting normal to the shearing surface (negative for compression, disregarded for tension) and ε_V^p is the peak strain in shear, calculated as:

$$\varepsilon_V^p = \frac{1 + \nu^k}{E^k}(f_{v0} + |\sigma_n|\mu_0) \tag{20}$$

The stress–strain curves resulting from the constitutive relations adopted are illustrated in Fig. 3.

4. Calculation process for nonlinear analysis

The method described for the analysis of the cell is combined with the damage models for the cell components and implemented as a plane stress nonlinear constitutive model for the FEniCS finite element platform [3]. The modelling approach essentially comprises a serial two-scale analysis of a masonry panel. The interaction of the cell components is modelled in the micro-scale for deriving the stresses in the cell, or the macro-scale.

In keeping with the failure mechanisms encountered in regularly bonded masonry walls, the integrity variables for reducing the stiffness of the components are evaluated in prescribed directions only. As such:

a) head joints are checked for tensile and compressive damage in x
b) units are checked for tensile damage in x and for compressive damage in y
c) cross joints are checked for tensile and compressive damage in y
d) bed joints are checked for tensile damage in x, tensile and compressive damage in y and for shear damage in xy

The evaluation of the integrity variables in orthogonal directions is equivalent to an orthotropic Rankine failure criterion. This approach reduces computational complexity and produces more easily interpreted numerical results. The stiffness reduction is applied in an isotropic fashion, meaning that the integrity variables reduce the stiffness of each components in all directions, and it is irreversible, meaning that reduction of the strain does not lead to an increase in the integrity. The integrity variables are multiplied with the stress components in eq. (1), (2), (3), (4) and (5) for calculating the actual stress. Thus damage is not expressed on the macro-scale of the masonry but only on the micro-scale of the components.

The bandwidths h used in the constitutive laws (eqs. (13), (15) and (17)) are dependent on the dimension d of the component in the direction of damage evaluation, the total dimension of the periodic unit cell D in the direction being evaluated (Fig. 2) and on the characteristic element length l, namely the square root of the element surface area:

$$h = \frac{d}{D}l \tag{21}$$

The values for d are:

a) $l_m/2$ for the head joints in tension and compression in x
b) units u_1 and u_2 in tension in x are assigned $(l_u/2 - l_m/2)$ and $l_m/2$ respectively, while in compression in y they are both assigned $h_u/2$
c) cross joints are assigned $h_m/2$ in tension and compression in y
d) bed joints are assigned $(l_u/2 - l_m/2)$ in tension in x, $h_m/2$ in tension and compression in y and $(l_u/2 - l_m/2)$ in shear in xy.
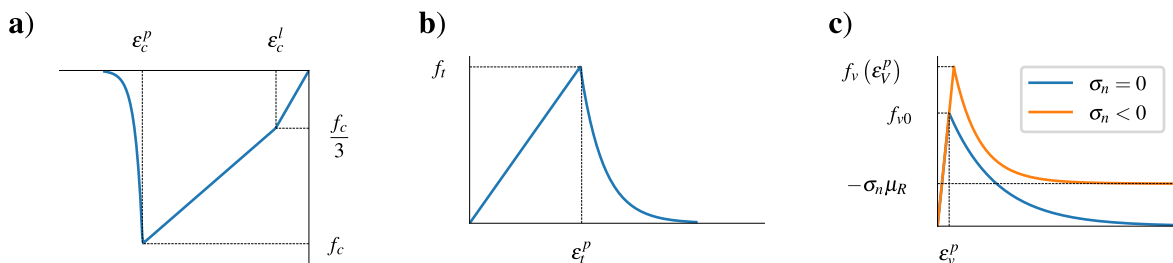

Fig. 3. Stress–strain curves in a) compression, b) tension and c) shear (under zero normal stress and under compression).

5. Model validation

5.1. Elastic analysis

Firstly, the elastic properties of the cell as predicted by the proposed model are compared against a FE micro-model benchmark. The FE analyses were executed in plane stress models of a periodic unit cell with imposed periodic boundary conditions [10]. The material and geometric properties used for the investigation are shown in Table 1. All parameters were kept constant apart from the Young's modulus of the mortar E_m, which was given a wide spectrum of values, ranging from 100 % to 0.1 % of the Young's modulus of the unit E_u. This range is intended to cover a wide range of stiffness ratios between units and mortar in order to achieve a comprehensive validation of the proposed homogenisation scheme. The lower limit of the investigated range is not representative of the elastic properties of any real undamaged mortar. Nevertheless, yielding of mortar in compression can result in a substantial reduction of stiffness. Therefore, even results using this low value have a bearing on masonry analysis.

The comparison of the results is shown in Fig. 4. The proportional reduction of the vertical Young's E_{yy} modulus is nearly identical to that of the shear modulus E_{xy}. This is expected due to the predominating influence of the deformation of the continuous bed joint in both vertical and shear deformation. Conversely, the reduction of the horizontal Young's modulus E_{xx} is slower owing to the interlocking of the units. The proposed model reproduces in-plane Young's and shear moduli as calculated through FE analysis with excellent accuracy. The in-plane Poisson's ratios are very well approximated for a great part of the investigated range, with the proposed model slightly underestimating these parameters for a ratio of E_u/E_m greater than 50. However, at that point the Poisson's ratios of the masonry are so low (~0.030) that the lateral deformation becomes insignificant. Overall, the accuracy of the proposed model in reproducing the results obtained from a FE benchmark is very high and is achieved with comparatively much reduced computational cost and ease of modelling. Further, the proposed model can provide easily interpretable results on the mean elastic stresses and strains in the components of the cell.

An additional verification of the stiffness results for the cell is executed through variation of the unit height h_u. The reference value for the value for the Young's modulus of mortar was used (Table 1). The comparison of the model with the FE benchmark are presented in Fig. 5. The horizontal and vertical Young's moduli are predicted with excellent accuracy throughout the investigated range. The shear modulus is overestimated for a unit length-to-height ratio (l_u/h_u) lower than 2, which is rare in brick masonry and uncommon in stone masonry built in running bond. The Poisson's ratios are slightly underestimated for the entire investigated range.

The stresses developed in the cell according to the homogenisation scheme are compared to the results obtained from the analysis using the reference values (Table 1). For executing the comparison, the stresses and strains in each FE subdomain corresponding to the masonry component were averaged. The comparison of the stresses is summarised in Table 2 and that of the strains in Table 3. The majority of the stress and strain components for each cell loading direction are calculated by the analytical model with very good accuracy, especially in the case of horizontal or vertical loading. A number of components, such as the vertical and shear stresses during horizontal loading of the cell, are not predicted with good accuracy. Further, the model assumes zero normal stresses and strains in all components during shear loading of the cell. However, these values of the component microscopic stresses and strains as predicted by the FE model, are very low relative to the macroscopic stresses and strains, thus rendering their influence on the macroscopic behaviour of the cell practically negligible. Further, it is demonstrated that the problem of alternating normal microscopic stresses in neighbouring components under the quarter cell assumption is of minor practical consequence.

The numerical efficiency of the model for FE computation is evaluated through a comparison of the results obtained from a linear elastic analysis of a masonry solid wall subjected to in-plane shear at the top equal to 1 N/mm^2 using the proposed homogenisation scheme and a FE micro-model. The wall was four units in length and 16 courses in height. The reference properties (Table 1) were assigned to the units and mortar. The homogenised model was composed of 426 triangular elements while the micro-model was composed of 8498 triangular elements. The number of elements in the micro-model is primarily dictated by the need to define separate mesh regions in the mortar joints, leading to a locally very fine mesh. The mesh for the homogenisation model was created in an average of 0.004 *sec*, whereas the micro-model required an average of 5.791 *sec*. The micro-model yielded a displacement of 0.3305 mm with an average analysis time of 0.137 *sec*, whereas the homogenisation model yielded a total displacement at the centre-top equal to 0.3382 mm (2.3 % overestimation) with an average analysis time of 0.024 *sec* (470 % improvement). The deformed shape and maximum principal strains obtained from the two models are presented in Fig. 6. The macroscopic maximum principal strains obtained from the homogenised model are equally suitable for indicating the locations of strain concertation as the strains obtained from the far more detailed micro-model.

Table 1

Material and geometric properties for validation of elastic property prediction. Reference values in parentheses.

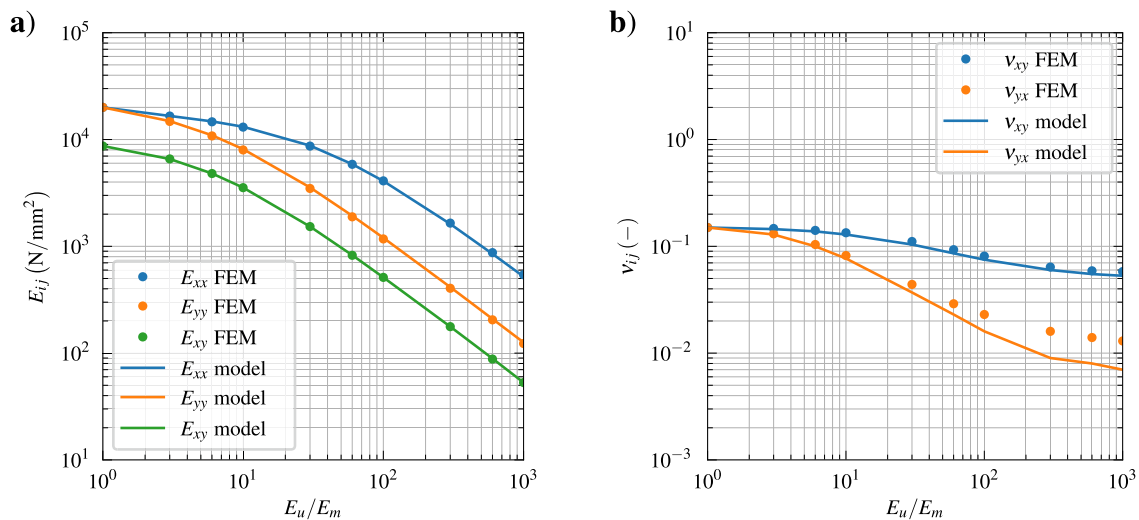| Units					
Units	Young's modulus	E_u	20,000	N/mm^2
	Poisson's ratio	ν_u	0.15	N/mm^2
	Length	l_u	210	mm
	Height	h_u	26 – 420 (52)	mm
Mortar	Young's modulus	E_m	20 – 20,000 (2000)	N/mm^2
	Poisson's ratio	ν_m	0.15	N/mm^2
	Head joint thickness	l_m	10	mm
	Bed joint thickness	h_m	10	mm

Fig. 4. Comparison of elastic properties predicted through finite element analysis and the proposed model for varying mortar stiffness: a) Young's and shear moduli, b) Poisson's ratios.
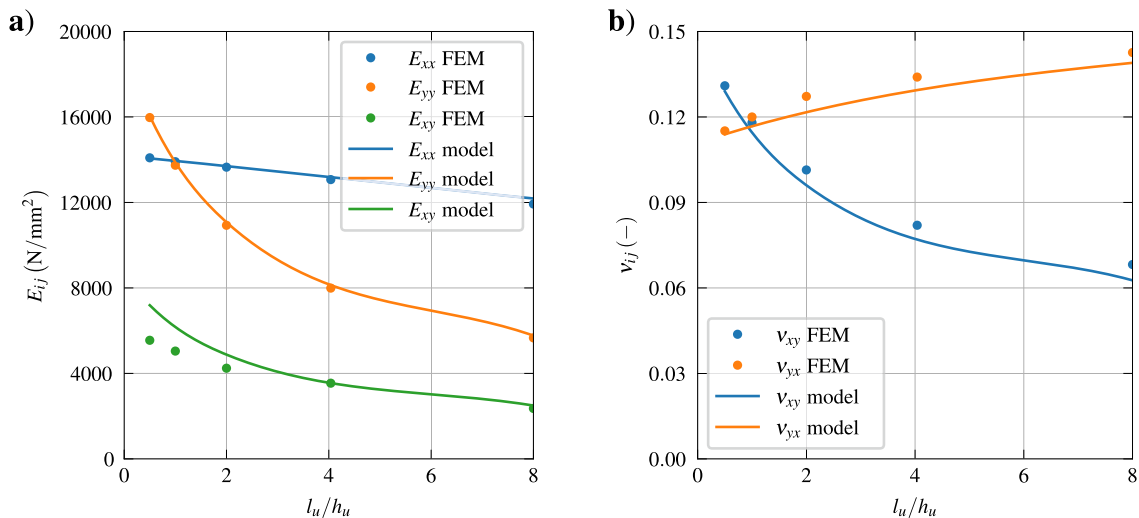

Fig. 5. Comparison of elastic properties predicted through finite element analysis and the proposed model for varying unit dimension ratios: a) Young's and shear moduli, b) Poisson's ratios.

Table 2

Comparison of elastic stresses predicted through finite element analysis and the proposed model. $\widehat{\sigma}_{ij}^{kl}$: ratio of analytical over FE component stress in ij for cell loading in kl. Percentages in parentheses indicate the ratio of the component microscopic stress over the macroscopic cell stress.

	$\widehat{\sigma}_{xx}^{xx}$	$\widehat{\sigma}_{yy}^{xx}$	$\widehat{\sigma}_{xy}^{xx}$	$\widehat{\sigma}_{xx}^{yy}$	$\widehat{\sigma}_{yy}^{yy}$	$\widehat{\sigma}_{xy}^{yy}$	$\widehat{\sigma}_{xx}^{xy}$	$\widehat{\sigma}_{yy}^{xy}$	$\widehat{\sigma}_{xy}^{xy}$
Unit	1.076 (108.8 %)	0.884 (-0.5 %)	1.363 (3.6 %)	1.076 (-2.4 %)	1.023 (102.2 %)	0.617 (0.0 %)	0.000 (1.8 %)	0.000 (2.8 %)	0.993 (100.7 %)
Bed joint	0.422 (32.4 %)	0.595 (-0.8 %)	1.426 (5.4 %)	1.198 (11.00 %)	0.994 (101.0 %)	0.181 (0.0 %)	0.000 (3.5 %)	0.000 (5.6 %)	1.002 (99.5 %)
Head joint	0.926 (94.7 %)	2.290 (5.0 %)	0.831 (0.8 %)	1.374 (-1.4 %)	0.256 (35.6 %)	0.031 (-0.4 %)	0.000 (-0.4 %)	0.000 (-3.0 %)	1.167 (85.8 %)

Table 3

Comparison of elastic strains predicted through finite element analysis and the proposed model. $\widehat{\varepsilon}_{ij}^{kl}$: ratio of analytical over FE component strain in ij for cell loading in kl. Percentages in parentheses indicate the ratio of the component microscopic strain over the macroscopic cell strain.

	$\widehat{\varepsilon}_{xx}^{xx}$	$\widehat{\varepsilon}_{yy}^{xx}$	$\widehat{\varepsilon}_{xy}^{xx}$	$\widehat{\varepsilon}_{xx}^{yy}$	$\widehat{\varepsilon}_{yy}^{yy}$	$\widehat{\varepsilon}_{xy}^{yy}$	$\widehat{\varepsilon}_{xx}^{xy}$	$\widehat{\varepsilon}_{yy}^{xy}$	$\widehat{\varepsilon}_{xy}^{xy}$
Unit	0.873 (83.7 %)	0.925 (-12.3 %)	1.040 (7.6 %)	0.991 (-7.2 %)	0.843 (49.1 %)	0.014 (0.2 %)	0.000 (0.3 %)	0.000 (0.6 %)	0.791 (23.0 %)
Bed joint	0.422 (32.5 %)	0.642 (-20.6 %)	1.923 (35.8 %)	0.605 (-12.2 %)	1.039 (373.0 %)	0.195 (0.0 %)	0.000 (3.0 %)	0.000 (8.0 %)	1.036 (175.4 %)
Head joint	0.926 (94.7 %)	0.248 (-45.6 %)	0.886 (5.2 %)	0.560 (-24.1 %)	0.323 (127.7 %)	0.046 (1.36 %)	0.000 (0.4 %)	0.000 (-6.0 %)	1.188 (153.5 %)
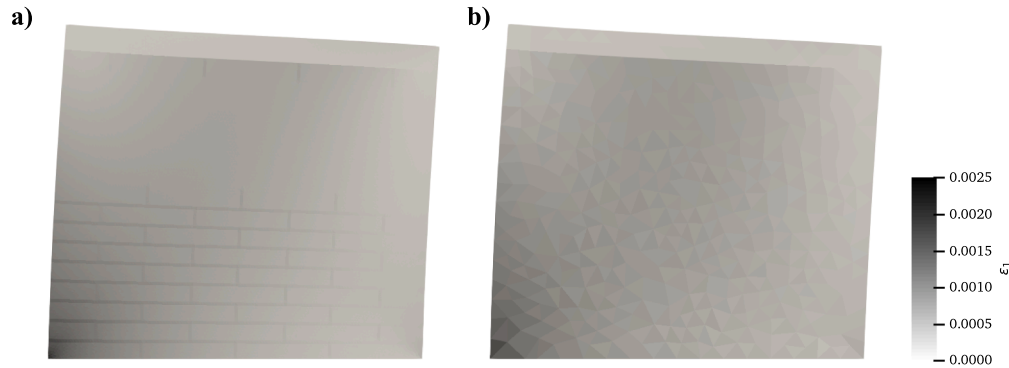
Fig. 6. Comparison of maximum principal strains obtained from a) micro-model, b) homogenisation model.

5.2. Nonlinear analysis

Secondly, the proposed model is validated in nonlinear analysis against the experimental results of [14,17]. These experiments involve quarter-scale masonry solid and perforated walls in running bond subjected to in-plane shear under varying levels of evenly distributed vertical stress. The walls were constructed using specially manufactured scaled bricks and a mortar with appropriately reduced aggregate size. The materials were extensively characterised through mechanical testing. The geometric and material properties of the units and mortar are presented in Table 4. The head joints were assigned the tensile properties of the unit-mortar interface in the x direction. The bed joints were assigned the tensile properties of the mortar in the x direction, the tensile properties of the unit-mortar interface in the y direction and the shear properties of the unit-mortar interface in the xy plane.

Table 4

Geometric and mechanical properties of units, mortar and unit mortar interface.

Units	Length	l_u	72.5	mm
	Height	h_u	12.5	mm
	Width	t_u	35.0	mm
	Young's modulus	E_u	4080	N/mm^2
	Poisson's ratio	ν_u	0.15	−
	Compressive strength	f_{cu}	−45.57	N/mm^2
	Tensile strength	f_{tu}	3.59	N/mm^2
	Compressive fracture energy	G_{cu}	45.57	N/mm
	Tensile fracture energy	G_{tu}	0.120	N/mm
Mortar	Head joint thickness	l_m	2.5	mm
	Bed joint thickness	h_m	2.5	mm
	Young's modulus	E_m	3500	N/mm^2
	Poisson's ratio	ν_m	0.20	−
	Compressive strength	f_{cm}	−7.44	N/mm^2
	Tensile strength	f_{tm}	1.05	N/mm^2
	Compressive fracture energy	G_{cm}	7.44	N/mm
	Tensile fracture energy	G_{tm}	0.111	N/mm
Unit-mortar interface	Tensile strength	f_{ti}	0.18	N/mm^2
	Tensile fracture energy	G_{ti}	0.013	N/mm
	Initial shear strength	f_{v0}	0.25	N/mm^2
	Initial friction coefficient	μ_0	0.815	−
	Residual friction coefficient	μ_R	0.770	−
	Tensile fracture energy	G_{ti}	0.013	N/mm
	Shear fracture energy	G_{vi}	0.300	N/mm

Two series of walls were tested in this campaign, one involving relatively squat masonry solid walls and one involving perforated walls with one window opening. The masonry was constructed with the bricks laid on a horizontal template on their stretcher faces and the mortar poured between the units. All walls were topped with a concrete beam for uniform load distribution. No lintels were provided in the perforated walls. All walls were tested in a cantilever configuration by allowing the top beam to rotate freely. Both series of walls were tested under varying levels of vertical stress, kept constant throughout each test, with a single repetition for each level of stress. The horizontal load was applied through an actuator pushing monotonically on one end of the top beam. The general layout of the walls is shown in Fig. 7. The in-plane shear load was applied from left to right.

The FE models of the solid and perforated walls consisted of 426 and 535 nodes and 780 and 958 triangular plane stress elements respectively. The top beam was assigned linear elastic properties and was, thus, not allowed to develop damage. The displacements at the base of the wall were constrained. In the present implementation of the model, a force-controlled nonlinear analysis of the masonry walls is performed. A constant vertical compressive stress is applied at the top while a shear stress is applied at the same location, increasing in magnitude for each load step.

The comparison of the experimental and numerical results in terms of peak shear stress under the different levels of vertical stress are presented in Table 5. The same results are further illustrated in Fig. 8 through normal-shear stress interaction diagrams. Overall, the agreement between the experimental and numerical results is good, particularly in the case of the perforated walls. In the case of the solid walls the numerical results appear to slightly overestimate the effective friction coefficient at the level of the structure [19]. This could be due to a higher friction coefficient in the bed joints or higher tensile strength of the head joints assumed in the numerical models compared to the actual values in the experimental specimens.

The comparison of the experimental and numerical force–displacement graphs is shown in Fig. 9. There is good agreement between experiments and numerical results in terms of initial stiffness for all experiments. The numerical models featured a more gradual degradation of the stiffness between the initial elastic part of the response and the peak compared to the experimental results. The cause of this discrepancy is not clear but is potentially linked to sliding of the base joint noted in the experiments or inaccurate simulation of the actual boundary conditions of the experiment.

The results of the model are compared with the experiments in terms of obtained failure mode. Tensile damage in the masonry is presented in terms of maximum principal strain ε_1 exceeding a threshold value. This threshold value is determined such as the resulting displacement is equal to 0.1 mm, which is the minimum crack width clearly detectable with the naked eye under normal conditions [24]. This is also an empirical limit for the assessment of soil-structure interaction damage below which cracking is deemed to be negligible [6]. Conversely, compressive damage is presented in terms of the integrity variable of the bed joint in compression I_c^b, as this is the main component of the cell failing in compression. The damage was recorded in the experiments by a single photograph at the end of the test. This simple approach for documenting damage is rudimentary and prone to subjectivity compared to the more recent trend of performing this task with digital image correlation [4,22], but can still provide useful information. Single crack lines running through joints are typically associated with tensile failure or slipping of the unit-mortar interface. Conversely, closely formed crack networks running through joints and units alike, as are often encountered near the compressed toe and the middle of the piers, are typically associated with compressive damage when vertical or biaxial failure when diagonal. The combined presentation of maximum principal strain and compression integrity variable allows for a simple and unambiguous interpretation and quantification of the numerical results and their comparison with qualitative experimental findings.

The results for the solid walls are presented in Fig. 10. Wall 2N20 presents a clear rocking behaviour, with a mostly horizontal crack at the base. This response is reproduced by the model, with the formation of a compressive failure zone visible at the compressed tow. Walls 3N40 and 4N50 exhibit similar response, with the formation of more diagonal tensile cracks and compressive damage at the compressed toe and closer to the point of application of horizontal load. The numerical model still predicts the formation of a horizontal crack at the base for the 3N40 and 4N50 cases, while the experimental results do not clearly indicate such damage. Overall, the
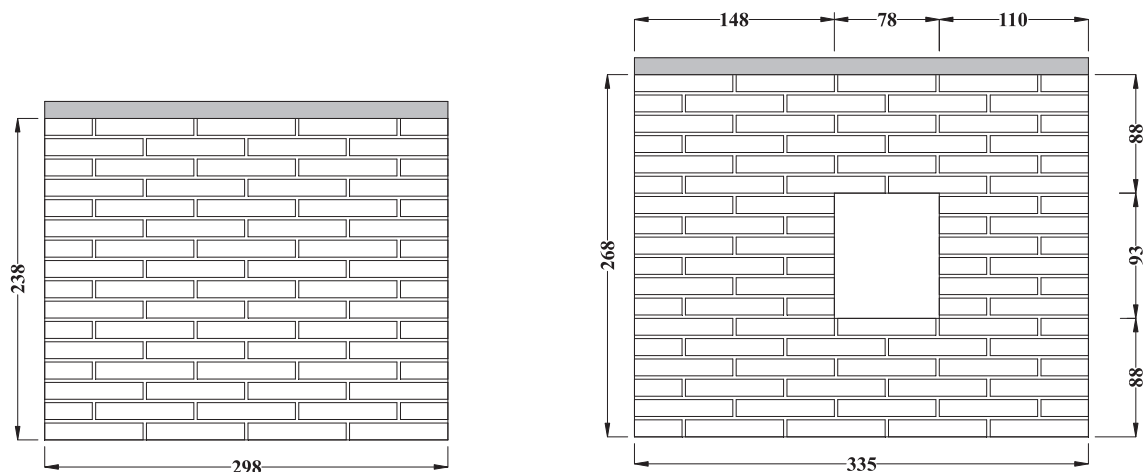

Fig. 7. Layout of tested panels: solid and perforated walls. Dimensions in mm.

Table 5
Summary of experimental and numerical results on solid and perforated walls subjected to in-plane shear.

Series	Specimen	Vertical stress σ (N/mm^2)	Experimental peak shear stress τ_{exp} (N/mm^2)	Numerical peak shear stress τ_{num} (N/mm^2)
Solid walls	2N20	1.942	1.119	1.175
	3N40	3.894	1.887	2.128
	4N50	4.764	2.105	2.501
Perforated walls	1V7	0.645	0.416	0.450
	2V13	1.132	0.649	0.716
	3V21	1.858	1.119	1.114
	4V30	2.540	1.116	1.359
	5V38	3.236	1.498	1.544
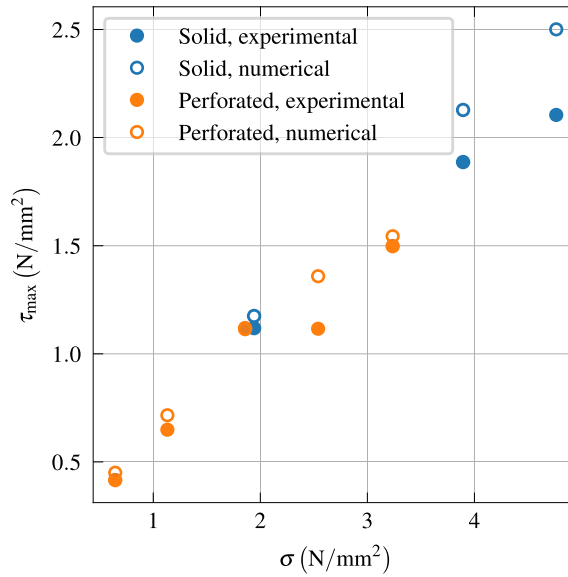
Fig. 8. Comparison of normal stress-peak shear stress interaction for experimental and numerical results.
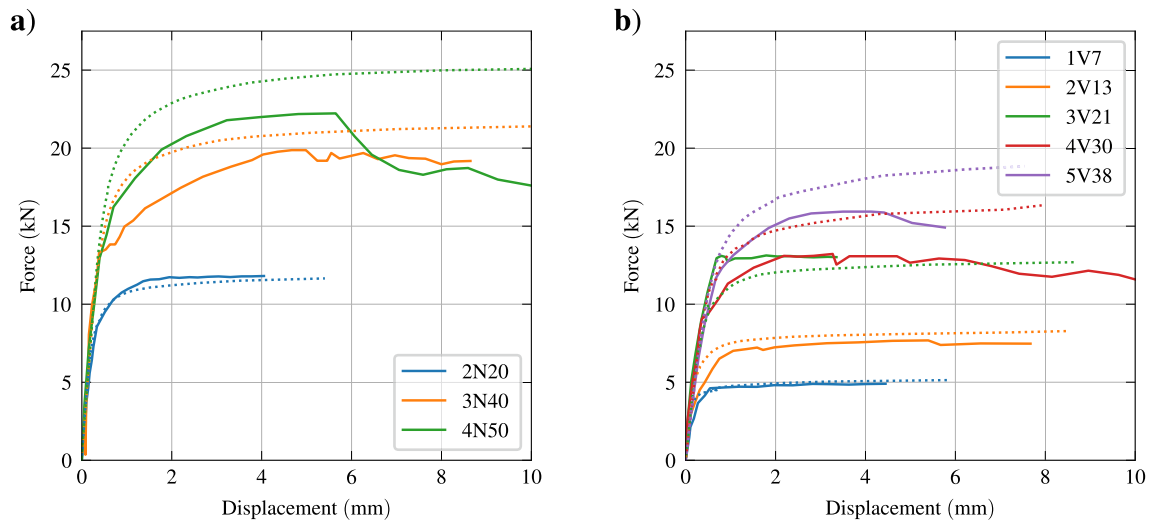
Fig. 9. Comparison of experimental (solid lines) and numerical (dotted lines) force–displacement graphs: a) solid walls, b) perforated walls.

2N20
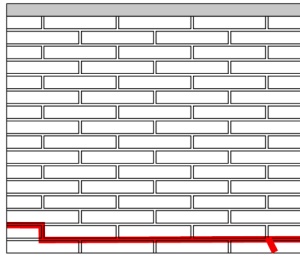
3N40
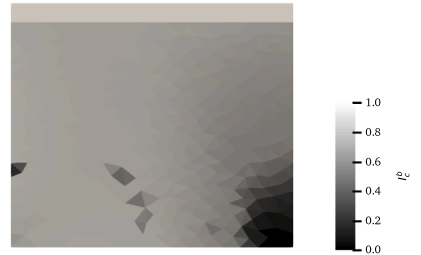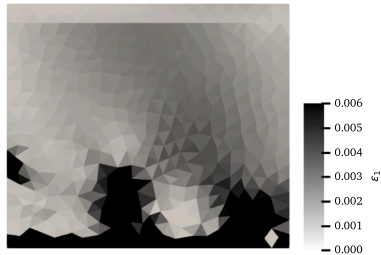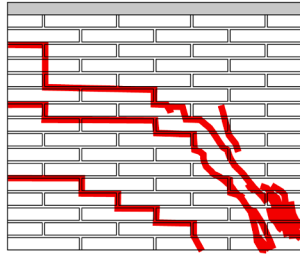
4N50
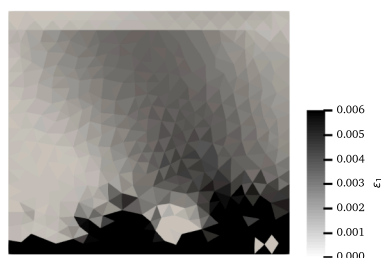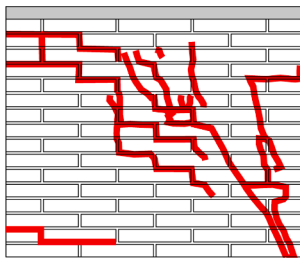
Fig. 10. Comparison of experimental damage pattern with maximum computationally-derived maximum principal strain ε_1 and integrity variable of bed joint in compression I_c^b in solid walls.

proposed model captures the main features of the experimentally derived failure patterns.

The results for the perforated walls are presented in Fig. 11. Overall, the formation of compressed struts on either side of the window are more clearly distinguishable from the developed compressive damage compared to the solid wall cases. Similarly, the opening also results in clearer formation of diagonal cracks. The main discrepancy between experiment and simulation is found in wall 1V7, where a purely rocking mode crack was documented in the test whereas additional diagonal cracks were obtained numerically. A further difference, in wall 3V21, is the formation of the rocking crack at the base of the left region of the lower spandrel in the model whereas these cracks are formed mostly at the top and base of the piers in the experiment. Apart from these differences, the computationally derived strains and integrity variables in compression can clearly interpret and quantify the damage while being in general agreement with the experimentally obtained failure patterns.

Overall, the model is capable of producing diagonal failure patterns typically encountered in masonry shear walls, especially those with openings, despite the orthotropic evaluation of the failure criteria for the individual components.

A sensitivity analysis was performed focused on the influence of the mortar and unit-mortar interface properties on the response of the 3V21 wall. The properties investigated are the tensile strength of the interface f_{ti}, the compressive strength of mortar f_{cm}, the initial friction coefficient of the interface μ_0 and the initial shear strength of the interface f_{v0}. These are the primary material parameters influencing the formation of bed joint tensile cracks, compressive strut hinges and the shear sliding at the bed joints. The results in terms of peak shear stress τ_{max} are presented in Fig. 12a. The hat operator indicates the normalisation of the material properties used and peak shear stress obtained from the analysis with the reference properties and results. Overall, variation of the normalised properties in the [0.5, 1.5] range resulted in a variation of the peak stress by less than 4 %, indicating the dependence of the response of shear walls more on boundary conditions and geometric layout rather than on material properties. The obtained force–displacement graphs for the variation of μ_0 are presented in Fig. 12b. While the peak shear stress was only marginally affected, the degradation of the stiffness following the elastic part of the response occurred more quickly for a reduced μ_0. Therefore, while the peak shear stress is not
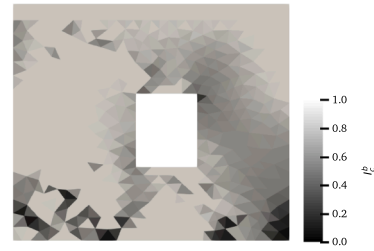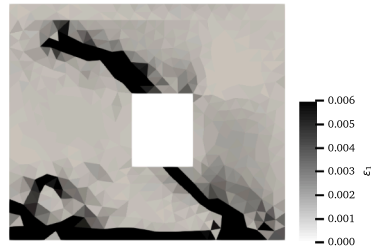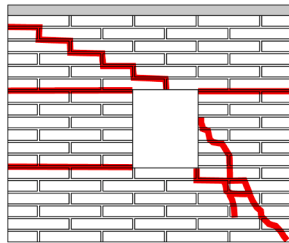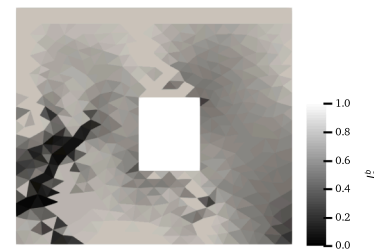
1V7
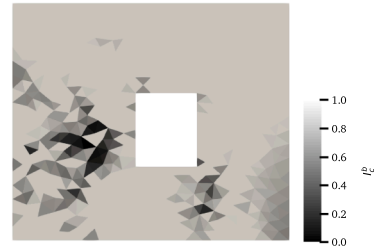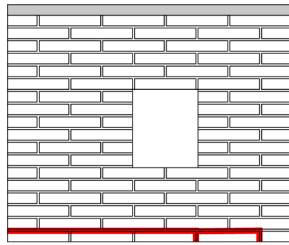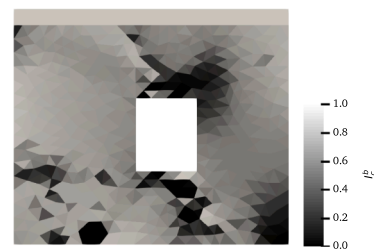
2V13
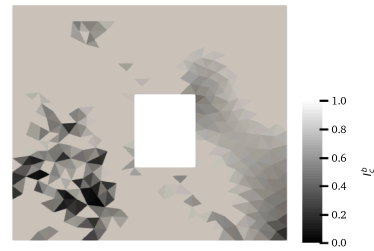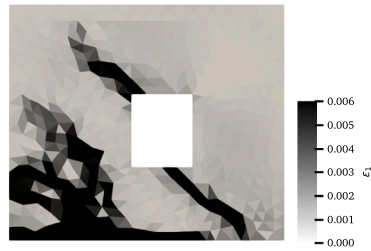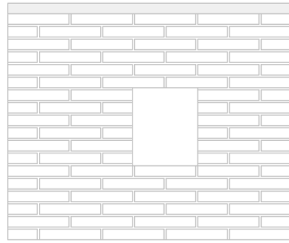
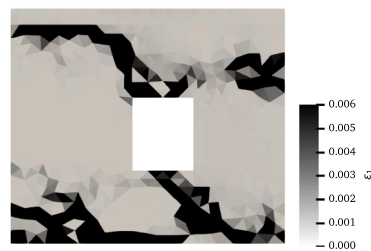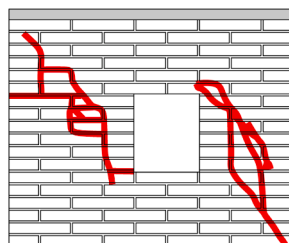**3V21**

4V30
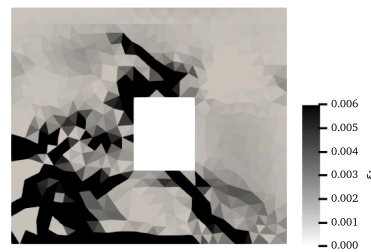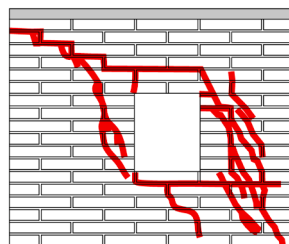
5V38

Fig. 11. Comparison of experimental damage pattern with maximum computationally-derived maximum principal strain ε_1 and integrity variable of bed joint in compression I_c^b in perforated walls. Failure mode for wall 2V13 was not recorded in the experiment.
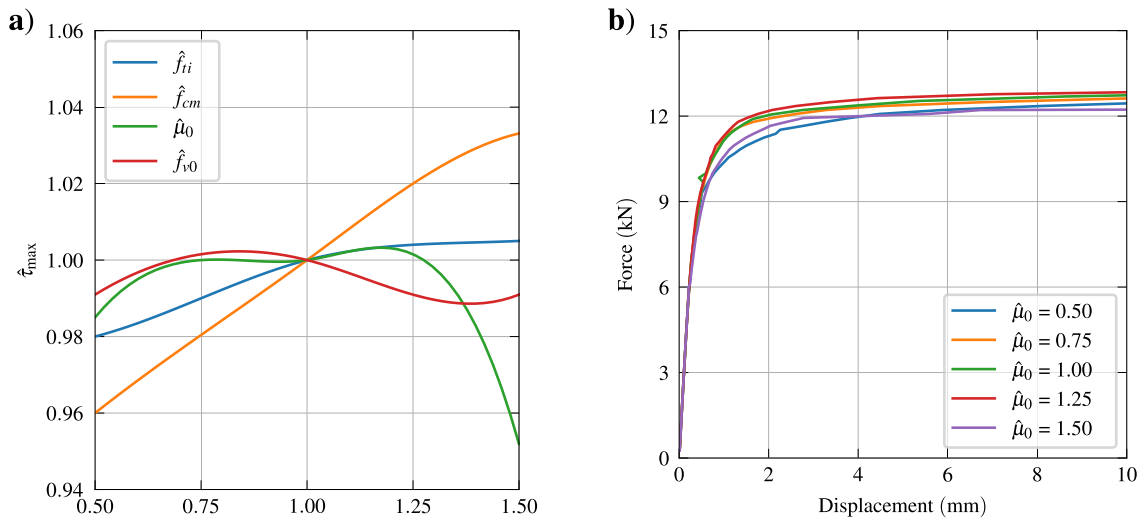
Fig. 12. Results of material parameter sensitivity analysis: a) normalised peak shear stress $\hat{\tau}_{\max}$, b) force–displacement graph.

very sensitive to material parameter change, certain details of the response can be affected by global or even local variations in material properties.

The obtained failure modes for wall 3V21 for a variation of the interface tensile strength f_{ti} are presented in Fig. 13. An increase in the tensile strength, while not significantly affecting the peak shear stress, causes a shift from a biaxial failure mode in the piers and spandrels to a failure mode dominated by rocking of the piers [9]. This shift leads to a clearer formation of mostly horizontal cracks at the base and top of the piers for $\hat{f}_{ti} = 1.50$.

Finally, a mesh sensitivity analysis was performed on the 3V21 case for evaluating the influence of the number of elements (n_{el}) on the response of the homogenised model compared to the reference case ($n_{el} = 958$). The results are illustrated in Fig. 14. The initial parts of the graphs are identical up to about 10 kN, corresponding to roughly 83 % of the peak force. Increasing n_{el} generally results in a small reduction in the peak force, equal to 5.8 % for $n_{el} = 8362$. Therefore, it is concluded that the response in terms of predicted peak force is relatively insensitive to mesh element size.
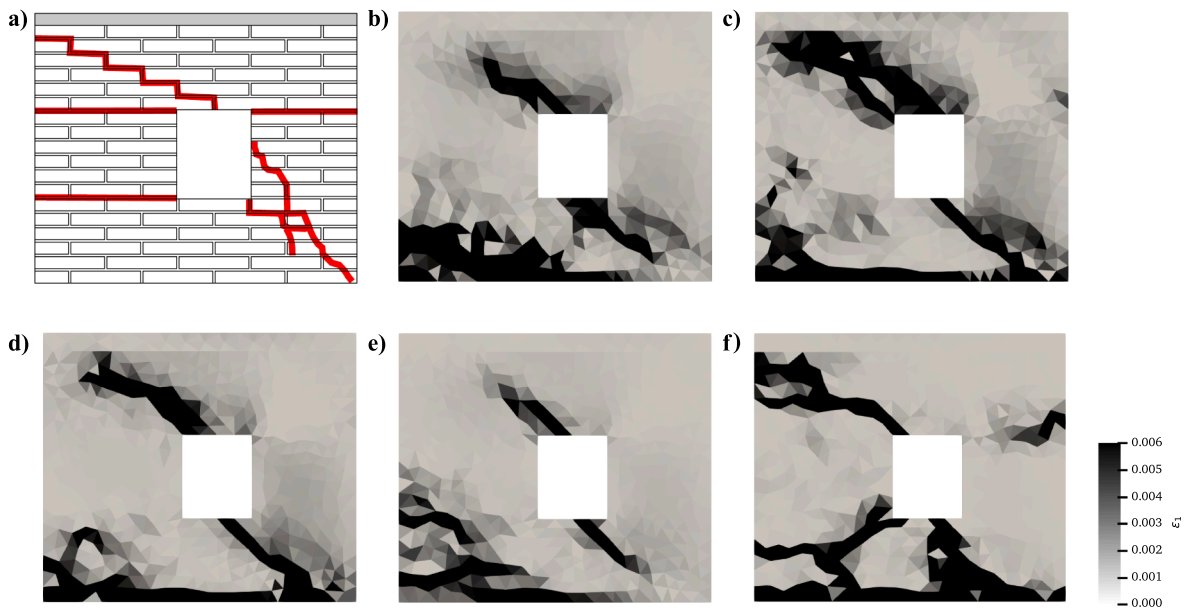

Fig. 13. Effect of interface tensile strength f_{ti} on obtained failure mode: a) experimental, b) $\hat{f}_{ti} = 0.50$, c) $\hat{f}_{ti} = 0.75$, d) $\hat{f}_{ti} = 1.00$, e) $\hat{f}_{ti} = 1.25$, f) $\hat{f}_{ti} = 1.50$.
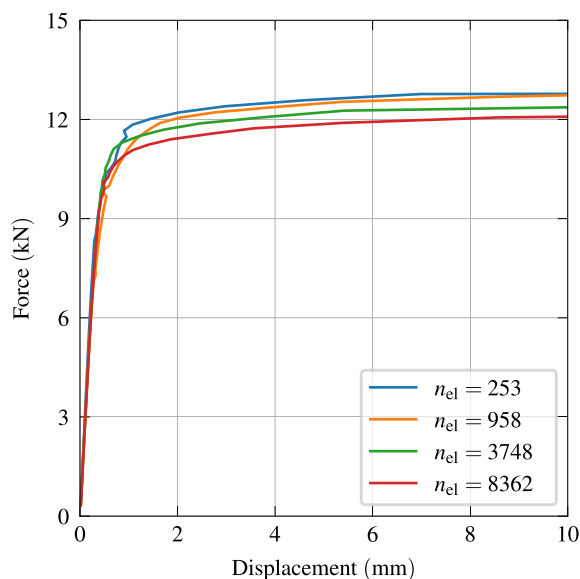
Fig. 14. Results of mesh sensitivity analysis: influence of number of elements (n_{el}) on force–displacement curves.

6. Conclusions

A nonlinear constitutive model for running bond masonry is proposed. This model is based on the micro-mechanical analysis of periodic unit cells using simple stress equilibrium and strain conformity between the components of the cell. The result is a low-cost approach for deriving stress, strain and damage in the components of the cell (units, bed joints, head joints) from the macroscopic strain in the cell. The model is implemented in a finite element context for simulating experimental tests on masonry shear walls.

The model provides highly accurate results in terms of predicting the orthotropic elastic properties of the masonry cell. Further, it is accurate in predicting the shear strength of solid and perforated walls under vertical stress. It is capable of generating failure modes very close to those observed in experiments and provides readily quantifiable results for damage. The model's capacity for providing quantifiable results on stress, strain and damage in the components of the cell from a finite element macro-model allows the simple interpretation of complex damage patterns and failure modes in large panel structures.

Future work based on this model firstly includes the development of bespoke solutions for other common masonry typologies, such as Flemish bond walls or regularly bonded pillar structures, the background for which has been developed in previous work. Secondly, the micro-mechanical approach allows the modelling of mechanical intervention methods, such as plain and reinforced repointing or externally bonded reinforcement. Finally, expansion of the approach to account for out-of-plane effects will allow the analysis of panels in combined in-plane and out-of-plane shear.

Declaration of Competing Interest

The authors declare that they have no known competing financial interests or personal relationships that could have appeared to influence the work reported in this paper.

Data availability

Data will be made available on request.

References

[1] J. Aboudi, Mechanics of Composite Materials: A Unified Micromechanical Approach, Elsevier, Amsterdam, 1991.
[2] J. Aboudi, S.M. Arnold, B.A. Bednarcyk, Micromechanics of Composite Materials: A Generalized Multiscale Analysis Approach, Elsevier Science, 2013.
[3] Martin S.Alnæs, Jan Blechta, Johan Hake, August Johansson, Benjamin Kehlet, Anders Logg, Chris Richardson, Johannes Ring, Marie E. Rognes, Garth N. Wells. 2015. The FEniCS Project Version 1.5, Archive of Numerical Software 3(100).
[4] L.-E. Bejarano-Urrego, E. Verstrynge, G. Giardina, K. Van Balen, Crack growth in masonry: numerical analysis and sensitivity study for discrete and smeared crack modelling, Eng. Struct. 165 (February) (2018) 471–485.
[5] S. Briccoli Bati, G. Ranocchiai, L. Rovero, A micromechanical model for linear homogenization of brick masonry, Mater. Struct. 32 (February) (1999) 22–30.
[6] J.B. Burland, C.P. Wroth, Settlement of Buildings and Associated Damage, in: Pp. 611–54 in Settlement of Structures, Proceedings of the Conference of the British Geotechnical Society, 1974.
[7] M. Cervera, L. Pelà, R. Clemente, P. Roca, A crack-tracking technique for localized damage in quasi-brittle materials, Eng. Fract. Mech. 77 (13) (2010) 2431–2450.

[8] D. Abbati, A.M. Stefania, D.O. D'Altri, G. Castellazzi, S. Cattari, S. de Miranda, S. Lagomarsino, Seismic assessment of interacting structural units in complex historic masonry constructions by nonlinear static analyses, Comput. Struct. 213 (2019) 51–71.

[9] A. Drougkas, R. Esposito, F. Messali, V. Sarhosis, Analytical models to determine in-plane damage initiation and force capacity of masonry walls with openings, J. Eng. Mech. 147 (11) (2021) 04021088.

[10] A. Drougkas, P. Roca, C. Molins, Analytical micro-modeling of masonry periodic unit cells – elastic properties, Int. J. Solids Struct. 69–70 (2015) 169–188.

[11] A. Drougkas, P. Roca, C. Molins, Numerical prediction of the behavior, strength and elasticity of masonry in compression, Eng. Struct. 90 (2015) 15–28.

[12] A. Drougkas, P. Roca, C. Molins, Material characterization and micro-modeling of a historic brick masonry pillar, Int. J. Architect. Heritage 10 (7) (2016) 887–902.

[13] A. Drougkas, P. Roca, C. Molins, Nonlinear micro-mechanical analysis of masonry periodic unit cells, Int. J. Solids Struct. 80 (2016) 193–211.

[14] A. Drougkas, P. Roca, C. Molins, Experimental analysis and detailed micro-modeling of masonry walls subjected to in-plane shear, Eng. Fail. Anal. 95 (2019) 82–95.

[15] A. Drougkas, V. Sarhosis, A. D'Alessandro, F. Ubertini, Homogenisation of masonry structures subjected to seismic loads through matrix/inclusion micromechanics, Structures 38 (2022) 375–384.

[16] K. Grzyb, R. Jasiński, Parameter estimation of a homogeneous macromodel of masonry wall made of autoclaved aerated concrete based on standard tests, Structures 38 (2022) 385–401.

[17] Lobato Paz, Ernesto Miguel. Método Simple Para El Análisis de Muros de Obra de Fábrica Con Aberturas Bajo Solicitaciones En Su Plano, PhD dissertation, BarcelonaTech, Barcelona, 2009.

[18] Macorini, Lorenzo and Bassam A. Izzuddin. 2011. "A Non-Linear Interface Element for 3D Mesoscale Analysis of Brick-Masonry Structures." *International Journal for Numerical Methods in Engineering* 85(October 2010):1584–1608.

[19] G. Magenes, G.M. Calvi, In-plane seismic response of brick masonry walls, Earthquake Eng. Struct. Dyn. 26 (11) (1997) 1091–1112.

[20] T.J. Massart, R.H.J. Peerlings, M.G.D. Geers, Mesoscopic modeling of failure and damage-induced anisotropy in brick masonry, Eur. J. Mech. A/Solids 23 (5) (2004) 719–735.

[21] G. Milani, M. Valente, Failure analysis of seven masonry churches severely damaged during the 2012 Emilia-Romagna (Italy) earthquake: non-linear dynamic analyses vs conventional static approaches, Eng. Fail. Anal. 54 (2015) 13–56.

[22] N. Mojsilović, A.H. Salmanpour, Masonry walls subjected to in-plane cyclic loading: application of digital image correlation for deformation field measurement, Int. J. Masonry Res. Innovat. 1 (2) (2016) 165–187.

[23] Morandi, Paolo, L. Albanesi, Francesco Graziotti, T. Li Piani, A. Penna, Guido Magenes, Development of a Dataset on the In-Plane Experimental Response of URM Piers with Bricks and Blocks. Constr Build Mater 190 (2018) 593–611.

[24] G. Österberg, Topography of the layer of rods and cones in the human retina, Acta Ophthalmol. 13 (1935) 6–97.

[25] M. Pari, A.V. Graaf, M.A.N. Hendriks, J.G. Rots, A multi-surface interface model for sequentially linear methods to analyse masonry structures, Eng. Struct. 238 (2021), 112123.

[26] L. Pelà, M. Cervera, P. Roca, Continuum damage model for orthotropic materials: application to masonry, Comput. Methods Appl. Mech. Eng. 200 (9–12) (2011) 917–930.

[27] Jan G. Rots, Francesco Messali, Rita Esposito, Samira Jafari, V. Mariani, Computational modelling of masonry with a view to groningen induced seismicity, in: Pp. 227–38 in Structural Analysis of Historical Constructions: Anamnesis, diagnosis, therapy, controls - Proceedings of the 10th International Conference on Structural Analysis of Historical Constructions, SAHC 2016.

[28] S. Saloustros, L. Pelà, P. Roca, J. Portal, Numerical analysis of structural damage in the church of the Poblet monastery, Eng. Fail. Anal. 48 (2015) 41–61.

[29] M. Sousamli, Francesco Messali, Jan G. Rots. Constitutive model for the nonlinear cyclic behavior of brick masonry structures. Pp. 694–701 in Brick and Block Masonry - From Historical to Sustainable Masonry Proceedings of the 17th International Brick/Block Masonry Conference (17thIB2MaC 2020), July 5-8, 2020, Kraków, Poland, edited by J. Kubica, A. Kwiecień, and Ł. Bednarz. CRC Press.

[30] A. Taliercio, Closed-form expressions for the macroscopic in-plane elastic and creep coefficients of brick masonry, Int. J. Solids Struct. 51 (17) (2014) 2949–2963.

[31] B.V. Wilding, M. Godio, K. Beyer, The ratio of shear to elastic modulus of in-plane loaded masonry, Mater. Struct. 53 (2) (2020) 40.

[32] S. Zhang, K. Beyer, Numerical investigation of the role of masonry typology on shear strength, Eng. Struct. 192 (2019) 86–102.

[33] A. Zucchini, P.B. Lourenço, A micro-mechanical model for the homogenisation of masonry, Int. J. Solids Struct. 39 (12) (2002) 3233–3255.

[34] A. Zucchini, P.B. Lourenço, Mechanics of masonry in compression: results from a homogenisation approach, Comput. Struct. 85 (3–4) (2007) 193–204.

[35] A. Zucchini, P.B. Lourenço, A micro-mechanical homogenisation model for masonry: application to shear walls, Int. J. Solids Struct. 46 (3–4) (2009) 871–886.